

# 1 INTRODUCTION

## 1.1 THE ROLE OF SOLAR CELLS IN THE ENERGY TRANSITION

Climate emergency is happening before our eyes. The depth and intensity at which the planet Earth will be hit, and the severity of the threat to humanity might to this day be unknown, but the forces behind it are already set in motion. As stated in the latest IPCC report, “Global surface temperature will continue to increase until at least the mid-century under all emissions scenarios considered<sup>1</sup>.” In 2015, in an unprecedented international effort to address the climate crisis, the Paris agreements brought together 191 states to agree on maintaining the temperature rise to a maximum of 2°C.

The IPCC report in 2020 unfortunately casts a shadow to this prospect, as “global warming of 1.5°C and 2°C will be exceeded during the 21<sup>st</sup> century unless deep reductions in carbon dioxide (CO<sub>2</sub>) and other greenhouse gas emissions occur in the coming decades<sup>1</sup>.” The urgency to reduce greenhouse gas emissions has thus never been so high. To get a grasp of the challenge ahead of us, we can observe the annual global CO<sub>2</sub> emission per year, presented in Figure 1.1. This shows an exponential increase in CO<sub>2</sub> emissions since the mid-19<sup>th</sup> century, with emission peaks exceeding 40 billion tons per year in 2018 and 2019.

The energy sector represents over 70 % of the global greenhouse gas emissions<sup>2</sup> (see Figure 1.2). To reduce these greenhouse gases emissions, a global shift in the energy sector is thus needed. This shift is called the green energy transition, and it is defined by the IRENA (International Renewable Energy Agency) as the “pathway toward transformation of the global energy sector from fossil-based to zero-carbon by the second half of this century”<sup>3</sup>.

An essential lever in that direction is the development and upscaling of the renewable energy sector, to dramatically increase these energies’ share in the energy mix. Renewable energy sources such as solar, wind, geothermal or biomass energy indeed differ from fossil fuels - oil, natural gas and coal - in that they are naturally replenished on a human

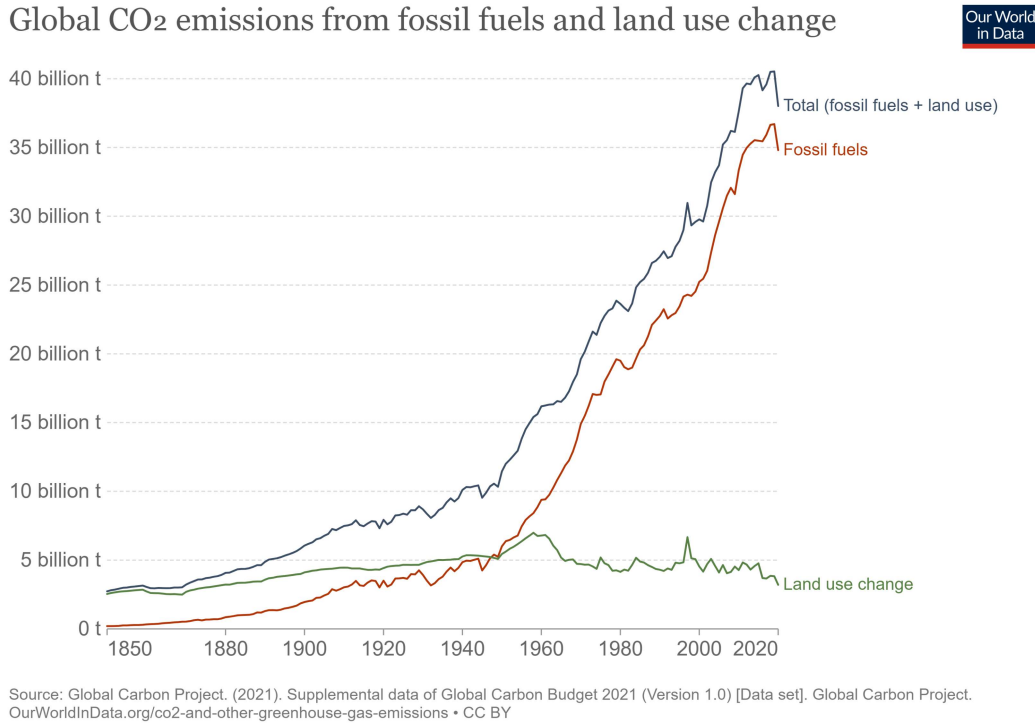


FIGURE 1.1. Annual CO<sub>2</sub> emissions worldwide, from 1850 to 2019. Reproduced from reference 2.

timescale. This allows for regular and prolonged use of energy, without compromising the availability of these energy resources for future generations.

The PhotoVoltaic (PV) sector is specifically promising with its total of 773 GW of installed capacity worldwide, of which 138 GW (18 %) were installed in 2020 alone<sup>4</sup>. With solar PV becoming the lowest cost-option for electricity generation in many parts of the world, policy support in the form of public investment is growing, as well as private investments.

At its core, a solar cell is a device which transforms solar energy into electrical energy. To do so, a solar cell consists of a photosensitive “active” layer, necessary to absorb photons from the solar spectrum. In semiconductors, these photons are absorbed and give rise to excitons, which are pairs of electrons and holes. The electrons and holes must then be transported through the active layer to their respective electrodes, where the current can be extracted.

Nowadays, silicon PV represents the highest share within the PV sector. While this technology might be efficient and reliable, the maximum theoretical efficiency limit of this technology has already been reached,

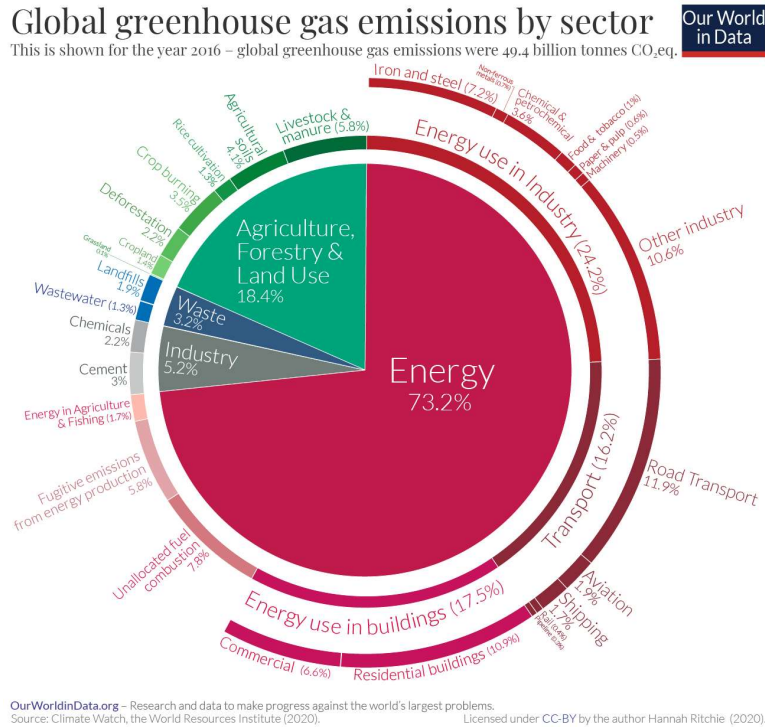


FIGURE 1.2. Global greenhouse gas emissions by sector, showing the energy sector as main contributor - data from 2016. Reproduced from reference 2.

and the silicon solar panels are not very flexible, making them unsuitable for proper integration in a variety of landscapes. The development of new PV materials with higher efficiencies, lower costs and with desirable properties such as material flexibility is a constant drive in research. In recent years, a specific type of material has attracted a lot of attention, namely the perovskite solar cells. With efficiencies rising dramatically in just a decade, these materials hold high promises in the PV sector.

## 1.2 PEROVSKITE SOLAR CELLS

The term “perovskite” describes a crystallographic structure. It was first used in 1839 by the German scientist Gustav Rose to name the mineral  $\text{CaTiO}_3$ <sup>5</sup>. Gustav Rose discovered this new mineral rock in the Oural mountains in Russia, and the word itself is an homage to the Russian mineralogist Lev von Perovski. In such a crystallographic structure, a monovalent A-cation sits in the centre of corner-sharing octahedra composed of divalent B-cations and monovalent X-anions. With its high bandgap of 3.8 eV<sup>6</sup>, the original perovskite  $\text{CaTiO}_3$  behaves as an insu-

lating material.

The first use of a perovskite structure in a solar cell device was shown by Miyasaka *et al.* in 2009<sup>7</sup>. There, the two studied perovskites were  $\text{MAPbI}_3$  and  $\text{MAPbBr}_3$ , coining the name of “organometal” perovskite, later labelled hybrid perovskites because of the mixed nature between the organic A ion and the inorganic B and X ions. In these structures, the inorganic framework consists of lead ( $\text{Pb}^{2+}$ ) as the divalent B-cation, and a halide species ( $\text{X}^-$ ) as the monovalent X-anion, leading to the general term of lead halide perovskites (see Figure 1.3). The A-cation can either be a methylammonium ( $\text{MA}^+$ ) molecule or a bulkier formadimium ( $\text{FA}^+$ ) molecule<sup>8</sup> in the case of hybrid lead halide perovskites, or a cesium ( $\text{Cs}^+$ ) cation<sup>9</sup> in the case of all-inorganic lead halide perovskites. Contrary to the oxide perovskites, the bandgap of these lead halide perovskites falls into the visible range, making them suitable for solar cell and LED applications.

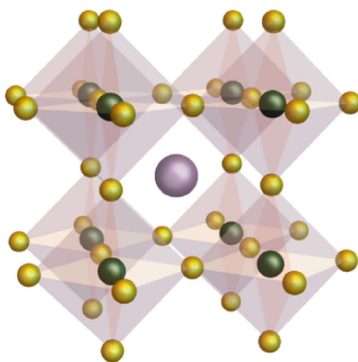


FIGURE 1.3. Perovskite  $\text{ABX}_3$  crystallographic structure, with A the monovalent cation shown in purple, B the divalent cation shown in green, and X the monovalent anion in yellow. In lead halide perovskites, the B-cation is  $\text{Pb}^{2+}$  and the X-anion is a halide, either  $\text{I}^-$ ,  $\text{Br}^-$  or  $\text{Cl}^-$ .

From the initial demonstration in a solar cell device in 2009, lead halide perovskite solar cells have shown an outstanding growth in Power Conversion Efficiencies (PCEs) over the recent decade, a trend which is unprecedented in the PV sector. The National Renewable Energy Laboratory (NREL) chart, which collects the record efficiencies of all PV devices, shows this dramatic increase (see Figure 1.4).

Part of the reason for the great success of lead halide perovskites comes from their bandgap tunability, where a simple modification of the halide species allows for a large variation in the bandgap energy: for example, in the methylammonium-based lead halide perovskites, the

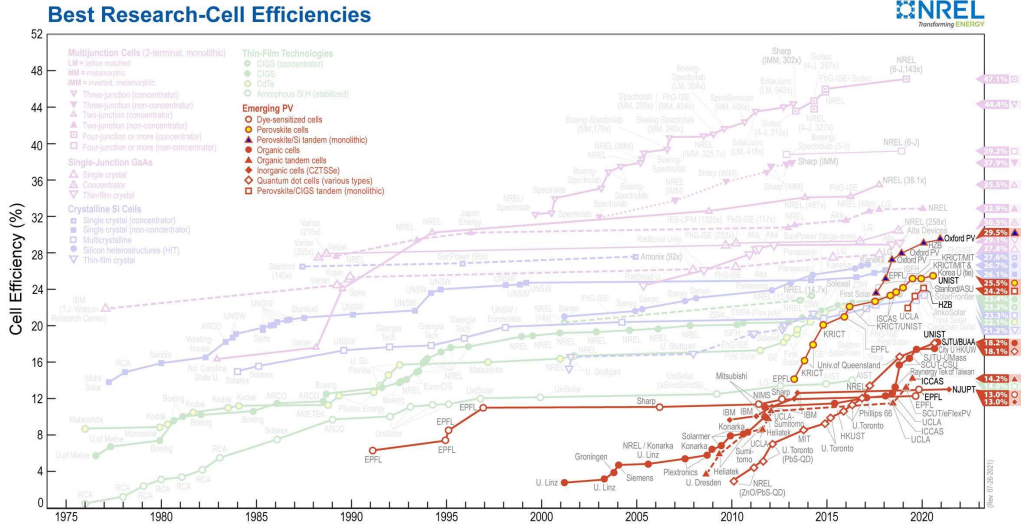


FIGURE 1.4. NREL chart presenting the record efficiencies of each of the PV technologies. The very rapid increase of the emerging PV sector over the last decade is shown in red, where perovskites play a crucial role. Reproduced from reference 10.

bandgap can span all the way from 1.6 eV for  $X = \text{I}$  to 2.9 eV for  $X = \text{Br}$ . An illustration of this bandgap tunability in the field of LED devices is shown in Figure 1.5.

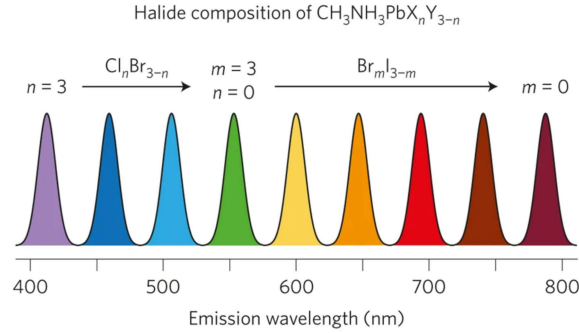


FIGURE 1.5. Bandgap tunability of the  $\text{MAPbX}_3$  perovskites series. Reproduced from reference 11.

Lead halide perovskites also present the key benefit of facile preparation, as they can be made with a variety of deposition techniques, ranging from wet chemistry (spin coating, drop casting, inkjet printing etc) to physical deposition by thermal evaporation. Low cost, reproducibility and large-scale homogeneity of the prepared perovskite layers are all key factors to consider for mass scale production of this technology.

Finally, a last key for the success of lead halide perovskites comes from their defect insensitivity. As mentioned above, perovskite layers can easily be prepared by a variety of fabrication methods. The resulting films often present high densities of structural defects, which could potentially reduce the efficiency of the resulting devices. In lead halide perovskites however, these defects have shallow energy levels<sup>12</sup> and thus do not contribute to non-radiative recombination of the electrons and holes. This defect insensitivity is essential to understand both the long carrier diffusion lengths (above 1  $\mu\text{m}$ )<sup>13</sup> and the high effective carrier mobilities (around 20  $\text{cm}^2 \text{V}^{-1} \text{s}^{-1}$ )<sup>14</sup> in these materials. The nature of the defects will be explored further in section 1.3.

Lead halide perovskite devices thus offer key benefits in terms of bandgap tunability, facile preparation methods, and outstanding efficiencies. There is however a major challenge ahead: while silicon PV panels last for more than 25 years, the lead halide perovskite devices are comparatively very instable. If we want these devices to take their full part within the solar technology portfolio to contribute to the increase of carbon-neutral energy capacities, this instability issue should thus be clearly addressed.

### 1.3 THE ISSUE OF EXTRINSIC INSTABILITY...

The instability of lead halide perovskites is not surprising, considering the low activation energy required in the reaction process from precursors to perovskite,  $\text{CH}_3\text{NH}_3\text{X}(\text{s}) + \text{PbX}_2(\text{s}) \rightarrow \text{CH}_3\text{NH}_3\text{X}_3(\text{s})$ . Using solution calorimetry, Ivanov *et al.* found the standard enthalpies of formation to be on the order of 5 kJ/mol, for the whole halide series,  $\text{X} = \text{I}, \text{Br}, \text{Cl}$ <sup>15</sup>. Interestingly, the standard Gibbs free energy of  $\text{CH}_3\text{NH}_3\text{X}_3$  is negative, which is commonly interpreted as an indication for the stability of the hybrid perovskite compared to its constituent halides. However, the main stabilisation factor is found to be the entropic contribution, which is larger than the small enthalpic contribution<sup>15,16</sup>. This situation makes the intrinsic stability of the lead halide perovskites less straightforward than the negative Gibbs free energy might initially suggest. Indeed, while in most reactions, the enthalpic contribution is considered the thermodynamically driving factor for the degradation reaction, in some specific cases, such as reactions involving gaseous phases, high temperatures or dissociation processes, and especially when the enthalpic contribution is low, the entropic factor can play a decisive role<sup>16</sup>. This is particularly

relevant for lead halide perovskites, which have been observed to degrade into the volatile gaseous phases of  $\text{CH}_3\text{X}$  and  $\text{NH}_3$ <sup>17</sup>, and  $\text{CH}_3\text{NH}_2$  and  $\text{HX}$ <sup>18</sup>. Thermal stress is thus one of the prominent environmental factors affecting lead halide perovskites stability. Another source of degradation for perovskites is humidity<sup>19,20</sup>, which can lead both to the formation of hydrated phases of the perovskite crystal, and/or to the desorption of the AX species, further degrading the perovskite layer into separate phases of AX and  $\text{PbX}_2$ . Other environmental damaging factors include oxygen exposure<sup>21,22</sup> and UV radiation<sup>23,24</sup> (see Figure 1.6).

While all of these environmental factors can lead to perovskite degradation, mitigation strategies have been developed: these include encapsulation strategies<sup>25</sup> but also passivation strategies in the bulk of the perovskite, in the grain boundaries or at the interfaces with the transport layers<sup>26</sup>.

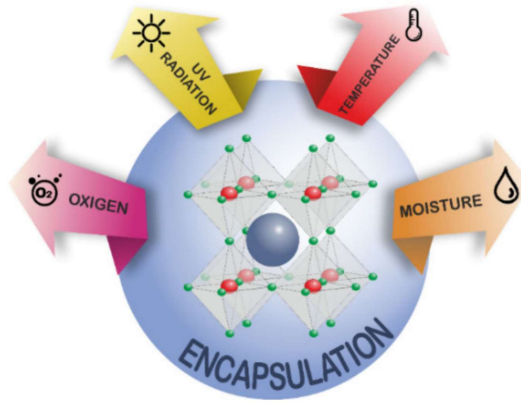


FIGURE 1.6. Schematic representation of different external factors affecting the stability of lead halide perovskites. Reproduced from reference 27.

Contrary to the most commonly-used PV materials, which are based on pure covalent bonding, the bond in lead halide perovskites also exhibits some ionicity<sup>12</sup>. Bearing in mind that ionic bonds are weaker in nature than covalent bonds, this helps to rationalize both the soft structure of the lead halide perovskites<sup>28,29</sup>, and the low formation energies for defects to occur in the lattice<sup>12,30,31</sup>. Some of the most common defects include Schottky defects, which are point defects formed when oppositely charged ions leave their lattice sites. Schottky defects occur in stoichiometric units so as to keep the charge balance in the perovskite lattice. In lead halide perovskites, these defects are associated with the formation of methylammonium vacancies, lead vacancies and halide vacancies<sup>32</sup>. The high concentration of these defect vacancies within the



perovskite lattice is an important contributing factor to ion migration within the perovskite devices. On top of the extrinsic instability issues mentioned above, ion migration thus poses a fundamental intrinsic instability challenge for perovskite solar cells.

#### 1.4 ... AND INTRINSIC STABILITY, A CLOSER LOOK AT ION MIGRATION

Ion migration is the process whereby an ion moves from its original position in the perovskite lattice to a new position within the perovskite lattice. This process happens through a hopping mechanism and can either be vacancy-mediated or interstitial-mediated. DFT calculations<sup>33</sup> show that the vacancy-mediated process has a lower activation energy, making it the most probable process within the lead halide perovskites. Schematic examples of vacancy-mediated ion migration of the halide ion, lead ion and methylammonium ion are shown in Figure 1.7 and 1.8. When calculating the respective migration energies of each of the individual ions  $\text{MA}^+$ ,  $\text{Pb}^{2+}$  and  $\text{I}^-$  in the case of  $\text{MAPbI}_3$ , Eames *et al.* find values of 0.84 eV, 2.31 eV and 0.58 eV, respectively<sup>33</sup>. Based on these calculations, the most mobile species should therefore be the halide species, while the lead ion is assumed to be the least mobile of the ionic species within the perovskite lattice.

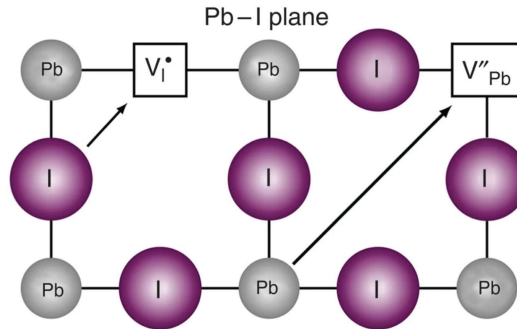


FIGURE 1.7. Schematic representation of ion migration of the iodide and lead ionic species towards their respective vacancies in the perovskite crystal lattice. Reproduced from reference 33.

Azpiroz *et al.* also use DFT simulations to calculate the migration activation energies in  $\text{MAPbI}_3$  and  $\text{MAPbBr}_3$ . In line with the results from Eames *et al.*, they also find  $E_a(\text{X}^-) < E_a(\text{MA}^+) < E_a(\text{Pb}^{2+})$  as the general trend, but the values are comparatively lower, with  $E_a$



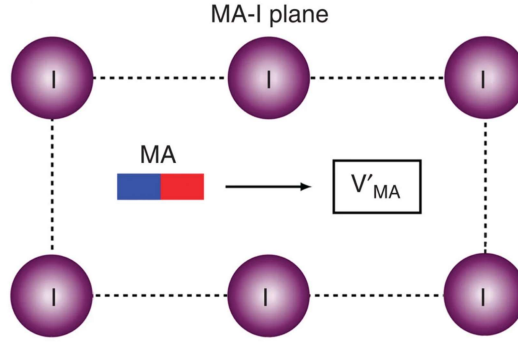


FIGURE 1.8. Schematic representation of ion migration of the methylammonium ionic species towards the methylammonium vacancy site in the perovskite crystal lattice. Reproduced from reference 33.

( $X^-$ )  $< 0.1$  eV for both the iodide and bromide ions<sup>34</sup>. Quantitatively, the results from DFT calculations thus differ and depend on specifics of the calculation model and computation arithmetic<sup>35</sup>, but qualitatively they still provide very insightful trends, useful for comparison between specific conditions. For example, Meggiolaro *et al.* find a lower formation energy for the formation of ion vacancies at the surface rather than in bulk<sup>36</sup>, while Haruyama *et al.* find that the substitution of  $MA^+$  by the bulkier  $FA^+$  cation increases the migration energies for both the halide ion and the A-cation<sup>37</sup>. DFT simulations screen systems on the order of 100 atoms, for timescales in the range of picoseconds<sup>38</sup>. To model larger systems and/or longer timescales, Molecular Dynamics (MD) simulations are more commonly adopted. Using classical MD, Balestra *et al.* study ion diffusion from the halide species in the all-inorganic  $CsPbX_3$  perovskites, and are able to distinguish the influence of the vacancy concentration from the influence of the migration activation energies<sup>39</sup>. In the methylammonium-based mixed-halide perovskites, Ruth *et al.* use Monte Carlo simulations to show that halide migration is a vacancy-mediated process in these systems<sup>40</sup>. Modelling of ion migration in lead halide perovskites thus offers a wealth of information in terms of defect formation energies and ion migration energies, which together can help rationalise some of the experimental findings.

Experimentally, there are two main avenues for the observation of ion migration in lead halide perovskites. The first avenue consists of the imaging and elemental characterisation techniques, which help visualise and characterise the ion migration processes<sup>35,41</sup>, for instance in terms of the nature of the migrating ions and their localisation within the perovskite layers. One of the clearest visualisation of the ion mi-

gration process was achieved by Luo *et al.*, who used a combination of nano X-Ray Fluorescence (XRF) and spatially resolved PL and were able to directly observe the migration of the bromide ion in a  $\text{MAPbBr}_3$  single crystal<sup>42</sup> (see Figure 1.9). Regarding the localisation of the mobile ions within the perovskites layer, Huang *et al.* used a combination of Kelvin Probe Force Microscopy (KPFM) and conductive atomic microscopy, and suggested that the mobile ions could aggregate near the device interfaces<sup>43</sup>. Yun *et al.* further used KPFM to show the enhancement of ion migration in the grain boundaries versus the bulk of the grains, in both formadium and methylammonium lead halide perovskites<sup>44</sup>. Using time-of-flight secondary-ion mass spectrometry, Zhang *et al.* could also study the degradation of  $\text{MAPbI}_3$  and  $\text{FAPbI}_3$  and profile the spatial distributions of the elements throughout full device stacks. They found that the iodide ion could transfer into the Hole Transport Material (HTM) and even through it to the silver electrode, and that degradation occurred faster in  $\text{MAPbI}_3$  compared to  $\text{FAPbI}_3$ <sup>45</sup>.

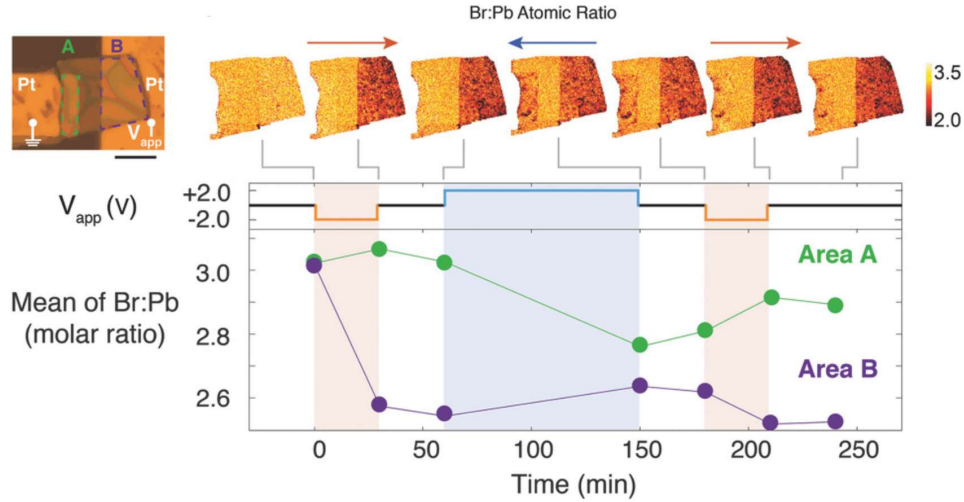


FIGURE 1.9. Nano-XRF measurement of the changes in elemental distribution in a  $\text{CH}_3\text{NH}_3\text{PbBr}_3$  single crystal under bias. Reproduced from reference 42.

Imaging and elemental techniques are thus critical to visualise the ion migration process, in order to probe which ions are moving within the devices and where they travel to. This set of techniques can also be used to study specific parameters of interest (such as film preparation conditions<sup>46,47</sup>, grain passivation effects<sup>48</sup>, etc.) and probe local variations within the perovskite layers, for instance bulk migration versus grain boundary migration. They do, however, lack to a large extent the quantification of the ion migration processes at hand, and are better at

characterising the migration processes from the heavy halide or cesium ions compared to the lighter organic cations such as  $\text{MA}^+$  and  $\text{FA}^+$ .

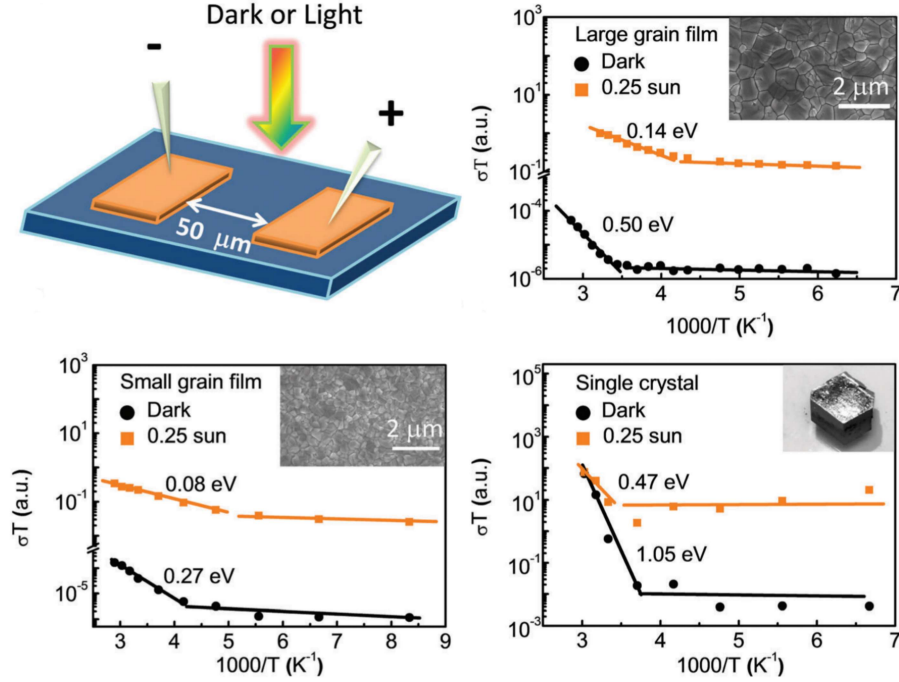


FIGURE 1.10. Quantification of the ion migration activation energy in  $\text{MAPbI}_3$  solar cells of various grain sizes, using temperature-dependent conductivity measurements. Reproduced from reference 49.

The second avenue of experimental techniques are temperature dependent transients measurements, such as conductivity and impedance measurements<sup>35,41</sup>. In these techniques, a physical property related to ion migration is measured at various temperatures. The characteristic timescales of the migration process are then recovered for each of these temperature transients, and finally, the activation energy for ion migration can be calculated by using the Arrhenius equation. Using impedance measurements, Bag *et al.* could compare the ion migration activation energy in pure  $\text{MAPbI}_3$  with that of the mixed cation system  $\text{MA}_x\text{FA}_{1-x}\text{PbI}_3$ , finding  $E_a(\text{MAPbI}_3) < E_a(\text{MA}_x\text{FA}_{1-x}\text{PbI}_3)$ <sup>50</sup>, while Xing *et al.* used temperature-dependent conductivity measurements to compare the migration activation energy in single crystals with those found for polycrystalline perovskite films of various grain sizes. There, they find an activation energy  $E_a$  for ion migration under dark conditions of 1.05 eV in the single crystal, of 0.50 eV in the films with large grains, and of 0.27 eV in the films with small grains (see Figure 1.10), i.e. a de-

crease in activation energy for the films with smaller grains<sup>49</sup>. This set of temperature-dependent transient techniques thus offers a key quantification benefit as they can be used to determine the migration activation energy. They do, however, lack the possibility of distinguishing which ionic species is migrating and thus often consider the range of possible ionic migration processes as a single averaged process. Besides this key issue of ion species discrimination, parameters other than the migration energy alone might be key to describe and understand the ion migration processes at play, such as the density of mobile ions or their diffusion coefficient. To fill in these gaps, we find Transient Ion Drift (TID) to be a suitable measurement technique to study the ion migration processes in lead halide perovskites.

## 1.5 THE TRANSIENT ION DRIFT TECHNIQUE

In this thesis, we make use of the TID technique to measure, quantify and analyse the ion migration processes taking place in lead halide perovskite solar cell devices.

TID relies on the application of a voltage bias to collapse the depletion layer within the perovskite semiconductor. The ions then diffuse through the device until they are homogeneously distributed. When releasing the voltage pulse, the ions will drift towards the electrode following the built-in electric field across the perovskite layer, changing the depletion width<sup>51</sup>. Considering the perovskite cell as a parallel-plate capacitor, this ion drift therefore leads to a change in the thickness of the dielectric layer (the depleted part of the perovskite layer). The evolution of capacitance over time thus results in a measurement of the ion dynamics. A more detailed description is provided below.

In Figure 1.11, we see a simplified scheme of the different steps taking place in the perovskite device during the TID measurement. In the first step, shown in Figure 1.11a, the device is in steady-state conditions and the ions are close to the electrodes of reverse polarity, where they accumulate. We then apply a voltage pulse  $V_0$  to the device, which redistributes the electrostatic field across the perovskite layer, changing the bands, as illustrated in Figure 1.11b. In TID measurements,  $V_0$  is chosen close to the built-in voltage  $V_{BI}$  of the device, such that the perovskite layer is fully depleted after application of this bias. The ions then start diffusing within the layer (Figure 1.11c-d) until they are fully homogenised, and flat band conditions are reached (Figure 1.11e). At

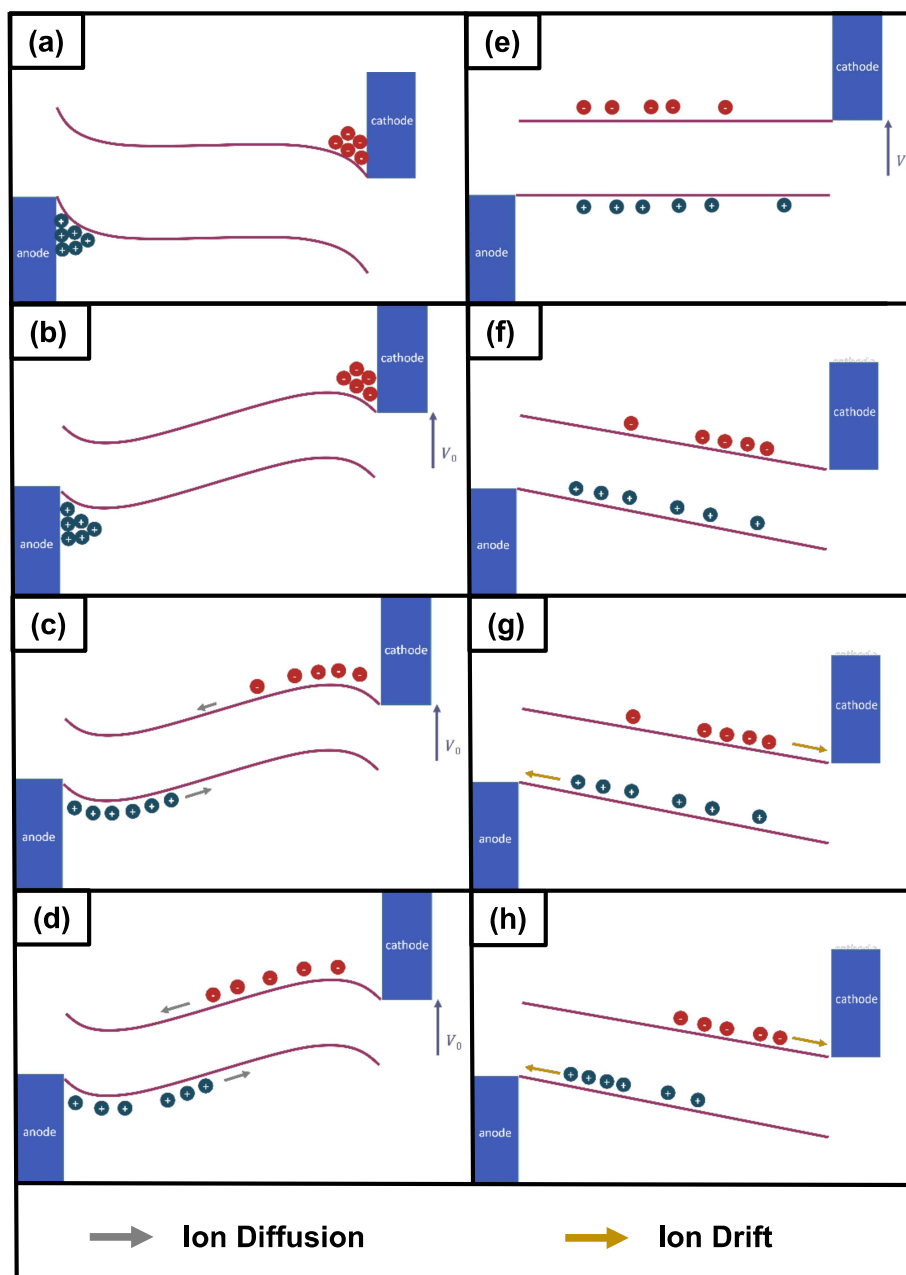


FIGURE 1.11. Schematic illustration of the different steps taking place in the perovskite layer of the solar cell device, after application of a voltage bias  $V_0$ , and successive release of this bias. After application of the voltage pulse, the depletion layer in the device is fully collapsed and the mobile ions diffuse within the perovskite layer, until they reach steady-state conditions. Then, the pulse is released, and the ions drift back to their original position – this is the time during which we record the ion drift dynamics with TID. Design inspired by M. Futscher<sup>51</sup>.

that point, we can say that the device has reached its new steady-state conditions. We then release the voltage pulse  $V_0$ , which results in the bands shifting by discharging of the capacitor (Figure 1.11f), and the ions starting to drift (Figure 1.11g-h) until they reach their initial position, accumulating at the electrodes (Figure 1.11a).

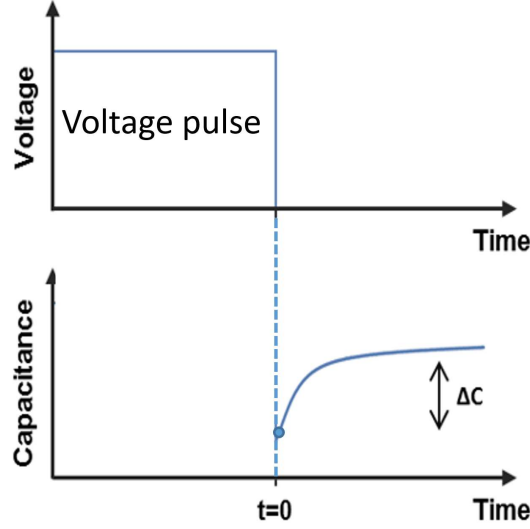


FIGURE 1.12. Measurement sequence of the TID technique. Design inspired by M. Futscher.

The measurement sequence is shown in Figure 1.12: a voltage pulse is first applied to the device, after which the capacitance of the sample is recorded as a function of time. Capacitance is thus recorded from the release of the voltage pulse, which we label  $t = 0$  (shown in Figure 1.11f), to the moment when the device reaches its steady-state conditions (shown in Figure 1.11a.). Capacitance is measured by applying a small perturbation voltage  $V_{AC} \sim 20$  mV to the perovskite device and measuring its impedance. The impedance signal is then converted to capacitance assuming a simple circuit model<sup>52</sup>.

TID allows for the discrimination of ion migration from a cation or an anion species. This can be determined by the sign of the capacitance transients. Specifically, in the case of a p-type semiconductor, a decay in capacitance transients signals anion migration and a rise in capacitance transients signals cation migration - and vice-versa in the case of an n-type semiconductor<sup>53</sup>. We recently found that this determination hinges on the assumptions made in the analysis (perovskite doping, only one depletion layer, ion drift dominant over diffusion), which might not be fulfilled in some devices. Three key parameters can be quantified with

TID: the activation energy for ions to migrate,  $E_a$ , the ion diffusion coefficient prefactor,  $D_0$ , and the mobile ion concentration,  $N_{ion}$ . These can be extracted using the following fitting procedure.

We first fit the capacitance transients to Equation 1.1, where  $C(t, T)$  is the capacitance at time  $t$  and temperature  $T$ ,  $C_\infty(T)$  is the steady-state capacitance at temperature  $T$ ,  $\Delta C_n(T)$  is the amplitude of the process  $n$  in the transient at temperature  $T$  and  $\tau_n$  is the lifetime of process  $n$ .

$$C(t, T) = C_\infty(T) + \sum_n \Delta C_n(T) \exp\left(\frac{-t}{\tau_n}\right) \quad (1.1)$$

Specifically,  $C_\infty(T)$  is extracted from the measurements directly from the steady-state capacitance, before the algorithm is allowed to find the best values for  $\Delta C_n(T)$  and  $\tau_n$ . As Equation 1.1 shows, the fit function can be adapted to contain any number of exponential terms needed to resolve the full dataset of capacitance transients, where each of these exponential terms represents one specific ion migration process  $n$ , with its own mobile ion concentration  $N_{ion(n)}$ , diffusion coefficient  $D_{0(n)}$  and migration activation energy  $E_{a(n)}$ .

Once we have extracted  $\tau_n$ , it can be rewritten as a function of the activation energy  $E_{a(n)}$  and of the ion diffusion coefficient prefactor  $D_{0(n)}$ , following Equation 1.2:

$$\tau_n = \frac{k_B T \epsilon \epsilon_0}{q^2 N_D D_{0(n)}} \exp\left(\frac{-E_{a(n)}}{k_B T}\right) \quad (1.2)$$

where  $k_B$  is the Boltzmann constant,  $\epsilon$  is the perovskite permittivity,  $\epsilon_0$  is the vacuum permittivity,  $q$  is the elementary charge and  $N_D$  is the doping density. Using Equation 1.2, we thus retrieve both  $D_{0(n)}$  and  $E_{a(n)}$  for each of the  $n$  processes.

Finally, the fitted  $\Delta C_n(T)$  parameters are used to determine the ion concentration  $N_{ion(n)}(T)$  using Equation 1.3:

$$N_{ion(n)}(T) = 2 N_D \frac{\Delta C_n(T)}{C_\infty(T)} \quad (1.3)$$

This fitting procedure thus allows for quantification of  $N_{ion(n)}$ ,  $D_{0(n)}$  and  $E_{a(n)}$ , key parameters characterising the ion migration processes taking place in the lead halide perovskite solar cells studied within this thesis.

The following chapters illustrate the evolution of the fitting procedure to the TID datasets obtained, from single temperature transient fitting



(Chapter 2), to global transient fitting - i.e. fitting all temperature transients from a specific TID dataset in a “single” global step - (Chapters 3 and 4), and global transient fitting in combination with a genetic algorithm approach (Chapter 5). These different methods all rely on the same set of equations, themselves based on the same assumptions, which are detailed below.

To write the previous set of equations, several assumptions are necessary. We first assume that the electric field is mostly determined by the doping density, and that the ions only pose a small perturbation, i.e. that the depletion width is mostly governed by the electronic charge carriers, and only slightly affected by the migration of ions. We also assume that the electric field after application of the voltage pulse varies linearly within the perovskite bulk<sup>54,55</sup>, that the total ion density is conserved, and that the diffusion is negligible against drift.

With this powerful technique, both able to distinguish anion migration from cation migration and capable of quantifying the relative contributions to ion migration - in terms of activation energy, diffusion coefficient and mobile ion density - we can explore a wide range of perovskite materials and shed light on the underlying ion migration processes.

## 1.6 OUTLINE OF THIS THESIS

The research question driving this thesis is the following: "How can we reduce ion migration in lead halide perovskite solar cells?". We aim to answer this question by studying a range of different factors which might affect ion migration in these solar cells.

We first look at the effect of the perovskite composition, with two study cases: first, comparing the ion migration processes in the pure-halide systems of MAPbBr<sub>3</sub> and MAPbI<sub>3</sub> (Chapter 2); second, looking at the effect of the halide ratio in the mixed-halide MAPb(Br<sub>x</sub>I<sub>1-x</sub>)<sub>3</sub> perovskites (Chapter 3). We then explore the effect of crystallinity, by studying the impact of the grain size on ion migration in MAPbBr<sub>3</sub> solar cells (Chapter 4). Finally, we also explore the effect of the dimensionality of the perovskite, by adding a thin 2D perovskite layer on top of a 3D perovskite and studying how this affects ion migration in these 2D/3D heterostructures (Chapter 5).